On Physical Mechanisms Relevant to Flow Resistance in Textured Microchannels

S.E. Game,* E.E. Keaveny, and D.T. Papageorgiou

Imperial College London

M. Hodes

Tufts University

(Dated: January 11, 2018)

Abstract

Flow resistance of liquids flowing through microchannels can be reduced by replacing flat, no-slip boundaries with boundaries adjacent to longitudinal grooves containing an inert gas, resulting in apparent slip. With applications of such textured microchannels in areas such as microfluidic systems and direct liquid cooling of microelectronics, there is a need for predictive mathematical models that can be used for design and optimization. In this work, we describe a model that incorporates the physical effects of gas viscosity (interfacial shear), meniscus protrusion (into the grooves) and channel aspect ratio and show how to generate accurate solutions for the laminar flow field using Chebyshev collocation and domain decomposition numerical methods. While the coupling of these effects are often omitted from other models, we show that it plays a significant role in the behavior of such flows. We find that, for example, the presence of gas viscosity may cause meniscus protrusion to have a more negative impact on the flow rate than previously appreciated. Indeed, we show that there are channel geometries for which meniscus protrusion increases the flow rate in the absence of gas viscosity and decreases it in the presence of gas viscosity. In this work, we choose a particular definition of channel height: the distance from the base of one groove to the base of the opposite groove. Practically, such channels are used in constrained geometries and therefore are of prescribed heights consistent with this definition. This choice allows us to easily make meaningful comparisons between textured channels and no-slip channels occupying the same space.

* Email address for correspondence: s.game14@imperial.ac.uk

I. INTRODUCTION

Superhydrophobic surfaces that seemingly repel water can be constructed by introducing microscale features, such as grooves or pillars, on an otherwise flat surface [1]. While perhaps the most notable example, the lotus leaf [2], occurs naturally, with modern micro- and nanoscale fabrication techniques superhydrophobic surfaces can now be manufactured in laboratory environments [3]. The superhydrophobicity of these surface is owed to the liquid being in the Cassie state, where the spaces between grooves or pillars contain a vapor and, usually, an inert gas (we will henceforth use "gas" to describe the contents of the grooves). When the liquid is flowing, it experiences an apparent slip due to the presence of the liquid-gas interface [1]. As such, textured surfaces can be employed in continuous flow microfluidic channels to, in effect, reduce flow resistance and allow for larger volumetric flow rates for a given pressure gradient. Necessary conditions for the liquid to remain in the Cassie state are given in Lam et al. [4]. For cases in which the surface tension of the meniscus and atmospheric gas pressure are insufficient to support flow in the Cassie state, other means of doing so have been explored [5, 6].

Experimental work on such textured microchannels performed by Ou et al. [7] demonstrated that the same flow rate through a textured microchannel can be achieved by driving the flow with a significantly smaller pressure drop as compared to a standard smooth parallel-plate channel. The potential of textured microchannels has also been demonstrated for liquid metal-based cooling of electronics, as heat can be more effectively transported away from microchips using channels with superhydrophobic patterning [4].

Given the potential microfluidic applications for textured channels, there has been a substantial effort to develop mathematical models to quantify flow resistance for a given texture, and further, to find the optimal channel geometries and texture patterns. Many studies have idealized the gas-liquid interface as flat and neglected gas viscosity. For a laminar, Poiseuille flow through a parallel plate channel textured on one side with longitudinal ridges, Philip solved for the velocity field [8] and then integrated the solution [9] to determine the mean velocity as a function of solid fraction and hydraulic diameter-to-ridge pitch ratio. Philip also found analytic expressions for the velocity field and mean velocity for a number of other cases, including laminar Poiseuille flow through a circular tube textured with longitudinal ridges. In this case, the menisci were not flat, but their curvature matched that of the ridges.

Lauga and Stone [10] used Philip's results to provide an expression for slip length for the circular tube geometry where the ridges are oriented parallel to the flow.

In the case of flow between parallel plates for which there is a symmetric and periodic texturing on both channel boundaries, Teo and Khoo [11] solved dual series equations for the velocity field, for arbitrary values of the channel height-to-pitch ratio and solid fraction. They found that for a height-to-pitch ratio of 1 and a solid fraction of 0.25, the slip length for a channel with both walls textured is 31% greater than that of a channel with only one wall textured. They also determined asymptotic expressions for the slip length for both small and large values of the channel height-to-pitch ratio and solid fraction.

While these studies have provided much insight into the fundamental fluid mechanics of these flows, other physically-relevant effects, such as meniscus curvature and gas viscosity, also need to be accounted for to make a quantitative assessment of and eventually optimize actual devices. Detailed micro PIV experiments performed by Ou and Rothstein [12] and Tsai et al. [13] have demonstrated a strong correlation between the details of the fluid velocity near the liquid-gas interfaces and the overall decrease in flow resistance, highlighting the importance of meniscus curvature effects. Through a perturbation analysis, Sbragaglia and Prosperetti [14] have indeed shown that meniscus curvature does impact the effective slip length. In particular, they find that the relationship between meniscus curvature and slip length sensitively depends on the channel height-to-pitch ratio. For relatively large height-to-pitch ratios (>1), the proportionally small increase in liquid domain area gained by meniscus deflection is overcome by the increase in shear stress at the ridge level. Hence, the flow rate decreases with an increased meniscus deflection (into the groove). The reverse is true for small height-to-pitch ratios. More recently, Teo and Khoo [15] used finite element methods to solve this problem for arbitrary, but constant, meniscus curvatures in the shear-free meniscus case. They found that the slip length doubles when the meniscus is fully deflected (90°) compared to when it is flat, for a height-period ratio of 1 and solid fraction of 0.25.

The effect of gas viscosity was explored by Maynes et al. [16] in the case of a flat meniscus. They demonstrated analytically and experimentally its importance under certain physically realistic conditions. The analysis involved finding the velocity field of both the liquid and the gas, replacing the no-shear boundary condition with the continuity of velocity and shear stress over the liquid-gas interface. A dual-series solution was found in the gas phase, whereas a finite volume method was used to calculate the liquid velocity. They found that for a gas-

liquid viscosity ratio of 0.0097, the shear stress from the gas phase can have a significant effect on the flow resistance. For example, at a solid fraction of 0.031, ridge pitch to hydraulic diameter ratio of 1 and cavity depth to hydraulic diameter ratio of 0.1, the slip length is reduced by nearly 50% relative to the shear-free meniscus case. This result illustrates the importance of including the gas phase for accurate calculations of the slip length, even at small viscosity ratios. Ng et al. [17] produced more general results using eigenfunction series expansions, enabling the study of arbitrary gas-liquid viscosity ratios as well as the effect of molecular slip on the solid-liquid interface.

While the aforementioned studies have shown the individual importance of the additional effects of meniscus curvature and gas viscosity, their combined effect on flow resistance in textured channels has yet to be explored. In this paper, we describe a mathematical model that includes both of these effects and show how to solve it numerically using Chebyshev collocation methods, in combination with coordinate transforms to handle meniscus curvature and domain decomposition techniques to accurately capture changes in boundary conditions at the (solid-liquid-gas) triple contact line. Within this numerical framework each of the physical effects mentioned above can be easily incorporated and any combination of the effects can be explored for parallel plate, as well as finite channel cross-section geometries. We do not need to assume that the meniscus curvature is small, which is particularly relevant when considering liquid metals such as galinstan.

Using this computational approach, we show that gas viscosity can reverse the effect of meniscus protrusion on flow rate. In particular, for channel geometries in which the flow rate monotonically increases with meniscus protrusion angle in the shear-free case, a gas viscosity ratio of 0.01 can cause the flow rate to monotonically decrease with meniscus protrusion angle. We also use our approach to test the validity of the periodic channel model when applied to channels with a finite cross-section. For thin channels, we find that the flow given by the periodic channel model coincides with that of the finite channel at the center of the cross-section, as one might expect. However, when the channel height is comparable to its width we find that the periodic model completely breaks down and does not accurately describe the flow anywhere in the channel. Finally, through our examination of the parameter space, we identify several design criteria to allow textured channels to deliver optimal performance, including the usage of few, but large, gas regions, as well as the need to carefully choose their depth as to minimize the effects of gas shear stress and

maximize the cross-sectional area of the liquid.

The paper is organized as follows. In section II, we discuss the mathematical model, detailing the geometry, boundary conditions and governing equations of the problem. In section III, we develop our numerical framework. In section IV, we verify our method against results in the literature. In section V, we provide our results and, finally, in section VI, we give our conclusions.

II. MATHEMATICAL MODEL

A. Geometry and assumptions

Consider a steady, unidirectional, and fully-developed laminar flow of a liquid of viscosity μ_l through a channel bounded above and below by parallel plates textured with gas-filled grooves so that the liquid is in the Cassie state. One period of such a channel is depicted in Fig. 1(a). The total height of the channel including the grooves is h and we let δ denote the depth of the grooves and l denote the groove period. The grooves are longitudinal and taken to be aligned with the flow direction z. We consider the cases in which the channel cross-section is infinite and periodic in the transverse direction, and that in which the cross-section has a finite number of evenly spaced grooves (see Fig. 3).

The flow in the liquid is driven by an imposed pressure gradient $\nabla p_l = -G\mathbf{e}_z$, where G is constant. Due to flow unidirectionality, this is also the liquid pressure gradient at each cross-section. Thus, the pressure for each cross section is constant, and as a result, the meniscus comprising the liquid-gas interface is a circular arc with constant curvature K. We assume that the curvature changes due to pressure variations in the z-direction are sufficiently slow that meniscus curvature can be taken to be constant in the z-direction, and hence preserve the unidirectionality of the flow.

Between the ridges, we assume that there is flow of a gas with viscosity μ_g that is also steady, unidirectional, and fully developed. It is, however, not driven by an imposed pressure gradient, but by its mechanical coupling with the liquid through boundary conditions imposed at the liquid-gas interface. As in Maynes et al. [16], we assume that the gas domains are not exposed to the atmosphere, and therefore impose the constraint that there is no net gas flow. This is enforced by a constant pressure gradient in the gas which must be found

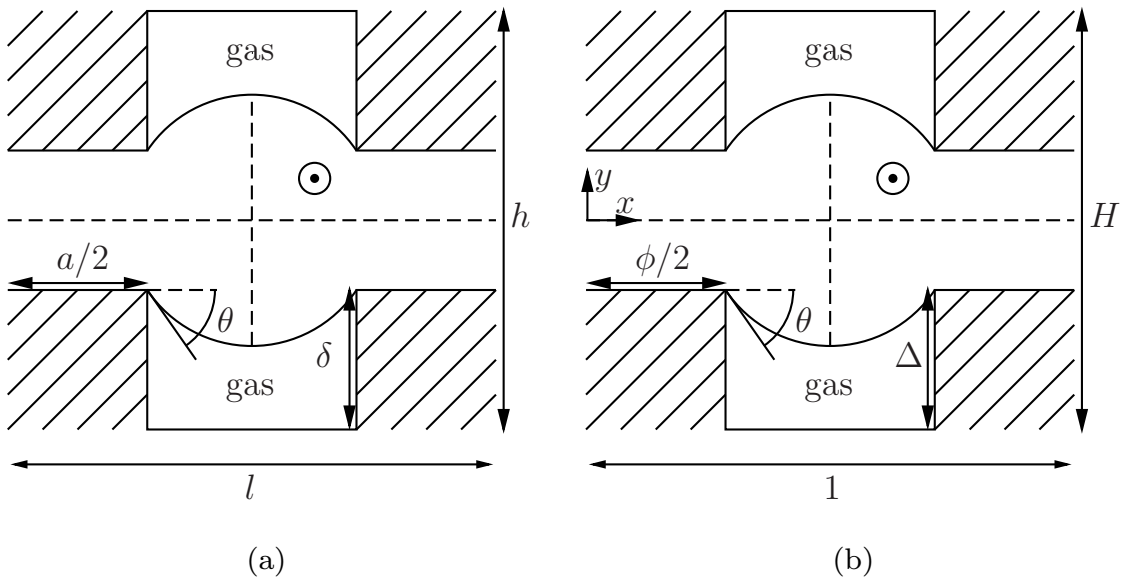

FIG. 1: A single period of the channel cross-section given in terms of (a) dimensional and (b) non-dimensional parameters.

as part of our solution.

B. Non-dimensionalization

The equations are non-dimensionalized using the groove period l to scale lengths, G to scale the pressure gradients in the gas and the liquid, and Gl^2/μ_l to scale the velocities of the liquid and gas phases. Using these, the following set of nondimensional parameters emerge:

$$\Delta = \delta/l, \tag{1}$$

$$H = h/l, \tag{2}$$

$$\phi = a/l, \tag{3}$$

$$\theta = \arcsin[Kl/2(1-\phi)], \tag{4}$$

$$\beta = \mu_g/\mu_l. \tag{5}$$

In the above expressions, Δ is the normalized gas depth, H is the normalized channel height, ϕ is the solid fraction of the textured boundaries, θ is the meniscus contact angle and β is the viscosity ratio. In Fig. 1(b) we illustrate one period of the channel cross-section, showing the

relevant non-dimensional parameters. In addition we have the dimensionless channel width W, which is an integer equal to the number of grooves on each bounding surface.

C. Governing equations

The velocities in the gas and liquid domains are denoted by $\boldsymbol{u}^{(g)}$ and $\boldsymbol{u}^{(l)}$ respectively, and satisfy the Navier Stokes equations:

$$\rho_i \left(\frac{\partial \boldsymbol{u}^{(i)}}{\partial t} + \boldsymbol{u}^{(i)} \cdot \nabla \boldsymbol{u}^{(i)} \right) = -\nabla p_i + \mu_i \nabla^2 \boldsymbol{u}^{(i)}, \tag{6}$$

$$\nabla \cdot \boldsymbol{u}^{(i)} = 0, \tag{7}$$

where i is either of g and l. Along with the viscosities described above, we have p_g and p_l and ρ_g and ρ_l describing the pressures and densities of the liquid and gas respectively.

Imposing the unidirectionality of the liquid and gas flows, $\boldsymbol{u}^{(i)} = (0, 0, w^{(i)}(x, y))$, non-dimensionalizing using the scalings introduced in the previous section, and maintaining the same notation for brevity, the governing equations become

$$w^{(l)}_{xx} + w^{(l)}_{yy} = -1 \tag{8}$$

in the liquid and

$$\beta(w^{(g)}_{xx} + w^{(g)}_{yy}) = \gamma \tag{9}$$

in the gas. Note that here and henceforth all quantities are dimensionless. The constant γ is the (unknown) pressure gradient that enforces the constraint

$$\iint_A w^{(g)} \mathrm{d}x\mathrm{d}y = 0, \tag{10}$$

where A is the cross section of any of the gas domains. This imposes that the net flow of gas is equal to zero as the ends of the grooves are assumed to be closed. The gas pressure gradient is always in the opposite direction to the liquid pressure gradient to counteract the gas velocity induced by the liquid along the meniscus.

To determine the liquid and gas velocity fields, we solve these equations subject to boundary conditions that impose no-slip at the solid-liquid and solid-gas interfaces, enforce velocity

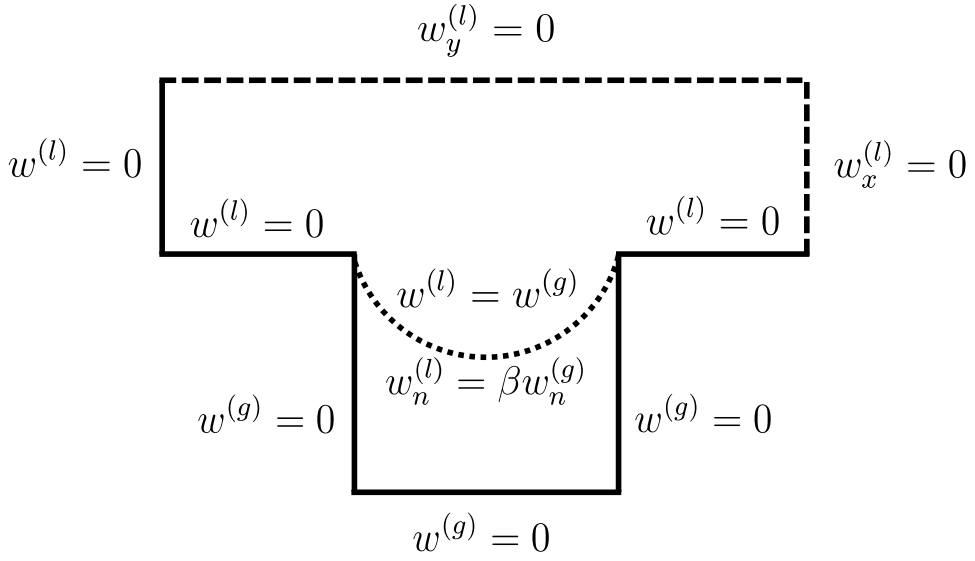

FIG. 2: The boundary conditions for the first period of a finite cross section with $W = 2$. Symmetry conditions are imposed along the dashed lines. The dotted line indicates the liquid-gas interface.

and shear stress continuity at the liquid-gas interface, and preserve the required symmetries. Specifically, at the physical boundaries of the domain, we have

$$w^{(g)} = 0 \qquad \text{(solid-gas)} \tag{11}$$

$$w^{(l)} = 0 \qquad \text{(solid-liquid)} \tag{12}$$

$$w^{(l)} = w^{(g)}, \qquad w_{\boldsymbol{n}}^{(l)} = \beta w_{\boldsymbol{n}}^{(g)} \qquad \text{(liquid-gas)} \tag{13}$$

on the three types of interfaces present in the domain (see Fig. 2). The unit vector $\boldsymbol{n}$ is the normal to the boundary of the liquid-gas interface and points out of the liquid domain towards the gas. Its appearance as a subscript denotes the directional derivative with respect to the normal direction.

Within the interior of the channel, we can identify one vertical and one horizontal line about which the flow should be symmetric. Therefore, for computational efficiency, we consider one quarter of the domain and impose appropriate boundary conditions along the symmetry lines. For the horizontal line, we impose the condition $w_y^{(l)} = 0$ while for the vertical line we take $w_x^{(l)} = 0$. An example of the symmetry lines is depicted by the dashed lines in Fig. 2 which shows a quarter of the domain with geometry having two grooves at

the bottom surface and two at the top; the position of the vertical symmetry line is adjusted accordingly depending on the even number of grooves on either surface.

After solving for the liquid and gas flows and gas pressure gradient, we can compute the liquid volumetric flow rate from the formula,

$$Q = \iint_S w^{(l)} \mathrm{d}x\mathrm{d}y, \tag{14}$$

where S is taken to be either a single period of the liquid domain or, if the channel has a finite cross-section, its entirety. The liquid volumetric flow rate will depend on all the non-dimensional parameters given previously, hence $Q \equiv Q(\Delta, H, \phi, \theta, \beta)$ for periodic channels and $Q \equiv Q(\Delta, H, \phi, \theta, \beta, W)$ for finite cross-section channels. The primary goal of this study is to quantify and understand these dependencies.

III. NUMERICAL FRAMEWORK

In this section, we describe the methods that we used to generate numerical solutions to the mathematical model described above. Our method consists of first decomposing the computational domain (the lower-left quarter of the channel cross section) into smaller subdomains using the natural boundaries provided by the (solid-liquid-gas) triple contact points. This allows us to numerically accommodate the sudden change in boundary condition at these points. After decomposing the domain, each subdomain is mapped to a canonical rectangular domain over which the governing equations are discretized using a Chebyshev collocation (spectral) method. After imposing continuity conditions to link together solutions from neighbouring domains, the result is a large, but sparse, linear system whose solution comprises the liquid and gas velocity fields and gas pressure gradients. We first describe our method for the more complicated case where the channel has finite cross-section, and then mention how to modify it to recover the periodic case.

A. Domain decomposition

Examining the boundary conditions described above, we see that at the triple contact points, there is an abrupt change in the boundary conditions, as well as a sudden change in curvature of the liquid domain boundary. Using these points to define boundaries as shown

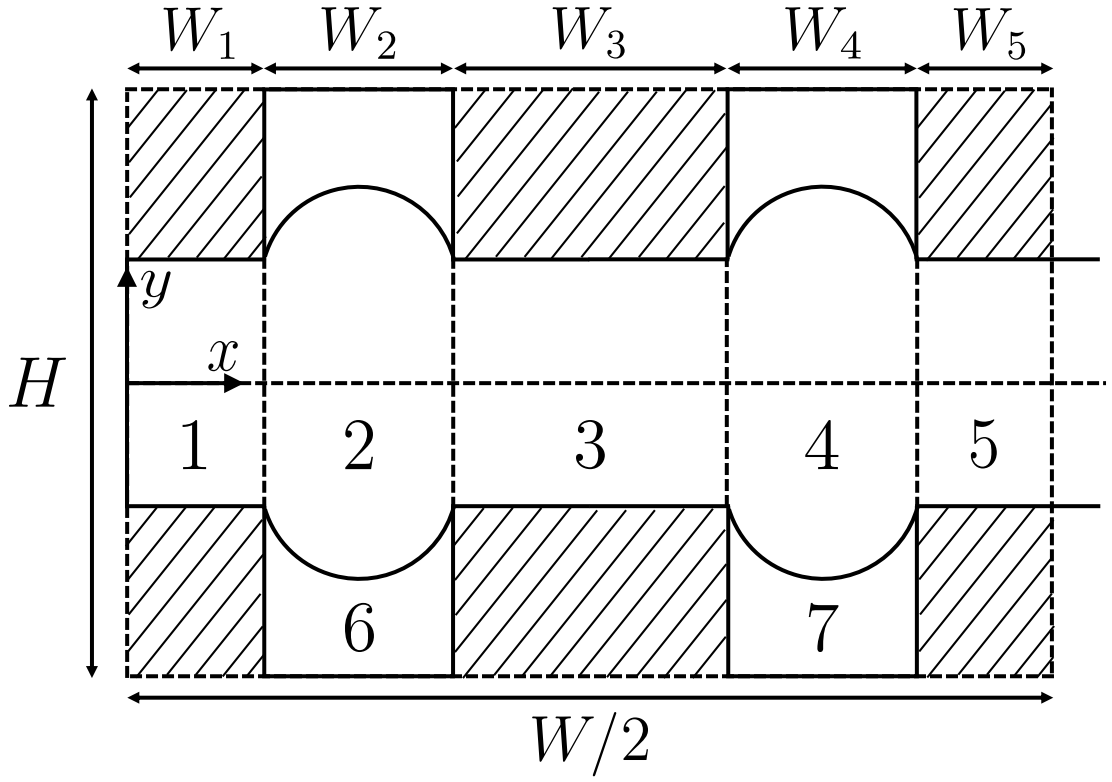

FIG. 3: A diagram showing how the domain is decomposed for the case where $W = 4$.

in Fig. 3, we can identify liquid subdomains in which the boundary condition imposed on the lower liquid boundary is continuous. For a channel with W grooves on each side, this will lead to $W + 1$ liquid subdomains and $W/2$ gas subdomains in the computational domain. Hence, there are a total of $3W/2 + 1$ subdomains that we index by m. Each subdomain will be one of five distinct subdomain types:

(A) The left-most liquid subdomain ($m = 1$) is unique in its boundary condition requirements and hence has a type to itself. In particular it requires a no-slip boundary condition on the left-hand side. See subdomain 1 in Fig. 3.

(B) This consists of liquid subdomains directly above gas subdomains (m is even and $m \leq W + 1$). These have gas-liquid interface boundary conditions on the lower side. See subdomains 2, 4 in Fig. 3.

(C) This consists of any liquid subdomain above a solid/liquid interface which is not at either end of our computational domain (m is odd and $1 < m < W + 1$). These have no-slip conditions on the lower side. Note that in the case $W = 2$ there are no

subdomain of this type. See subdomain 3 in Fig. 3.

(D) The right most liquid subdomain ($m = W + 1$) is unique in its boundary condition requirements and hence also has a type to itself. These have symmetry conditions on the right-hand side. See subdomain 5 in Fig. 3.

(E) The gas subdomains ($m > W + 1$) are the last type. These have gas-liquid interface boundary conditions on the upper side, and gas-solid interface conditions elsewhere. See subdomains 6, 7 in Fig. 3.

B. Coordinate transformations

After identifying the subdomains and classifying them based on their type, we map each one to the canonical $[-1, 1] \times [-1, 1]$ domain suitable for Chebyshev collocation. This transformation, coupled with domain decomposition, provides an effective way to accommodate meniscus curvature. Taking the origin in the physical (x, y) domain to be the point half way up the left-most channel wall (see Fig. 3), the transformed variables ξ_m and η_m for the liquid subdomains $m \leq W + 1$, are given by

$$\xi_m = \frac{2\left(x - \sum_{k=1}^{m-1} W_k\right)}{W_m} - 1, \qquad \eta_m = \frac{2y}{h(x)} + 1, \tag{15}$$

where W_k is the normalized horizontal width of the kth subdomain and $h(x)$ is the distance from the symmetry line of the channel to the lower boundary of the liquid domain. Henceforth, for clarity, within the context of one particular subdomain, we will write ξ and η to denote ξ_m and η_m respectively. Using the mapping (15), the derivatives of a function $F(x, y) = f(\xi, \eta)$ with respect to x and y are given by

$$F_x \mapsto f_\xi \xi_x + f_\eta \eta_x = \frac{2}{W_m} f_\xi - \frac{2(\eta - 1)}{W_m h_1(\xi)} h_1'(\xi) f_\eta, \qquad F_y \mapsto f_\xi \xi_y + f_\eta \eta_y = \frac{2}{h_1(\xi)} f_\eta, \tag{16}$$

where $h_1(\xi) = h(x)$. Hence, for subdomain types (A), (C) and (D), above a solid-liquid interface, $h_1(\xi) = H/2 - \Delta$. For subdomains of type (B), above a liquid-gas interface, we have

$$h_1(\xi) = \left[\left(\frac{1-\phi}{2\sin\theta}\right)^2 - \left(\frac{W_m \xi}{2}\right)^2\right]^{\frac{1}{2}} - \left[\left(\frac{1-\phi}{2\sin\theta}\right)^2 - \left(\frac{W_m}{2}\right)^2\right]^{\frac{1}{2}} + H/2 - \Delta. \tag{17}$$

and consequently,

$$h_1'(\xi) = \frac{-W_m^2 \xi \sin\theta}{2\left[(1-\phi)^2 - (W_m \xi \sin\theta)^2\right]^{\frac{1}{2}}}. \tag{18}$$

For the gas domains (subdomains of type (E)), the mapping from (x, y) to (ξ, η) is given by

$$\xi = \frac{2(x - \sum_{k=1}^{2m-2W-3} W_k)}{W_m} - 1, \qquad \eta = \frac{4y + 2H}{H - 2h(x)} - 1. \tag{19}$$

Note that the x substitution is the same as for domain $2m - 2W - 2$, which corresponds to the liquid domain directly above this gas domain. From this transformation, the derivatives of some function $F(x, y) = f(\xi, \eta)$ are given by

$$F_x = \frac{2}{W_m} f_\xi + \frac{2(\eta+1)}{W_m[H/2 - h_1(\xi)]} h_1'(\xi) f_\eta, \qquad F_y = \frac{2}{H/2 - h_1(\xi)} f_\eta. \tag{20}$$

C. Transformed equations and boundary conditions

Using the coordinate transforms described above, we rewrite the governing equations (8), (9) and (10), in terms of the coordinates ξ and η for each subdomain. For conciseness, all derivatives will be written in terms of x and y with the understanding that we can computationally transform these to (ξ, η) space via the derivative maps above to carry out the calculation. In practical terms, this means that each time an x or y derivative appears in the following, we would apply the discretized form of (16) (or (20) for a gas subdomain) as per Section III D. The following presentation corresponds to a channel with finite cross section.

In liquid subdomains (of type (A), (B), (C), (D)), we need to solve,

$$\frac{\partial^2 w_m}{\partial x^2}(\xi_m, \eta_m) + \frac{\partial^2 w_m}{\partial y^2}(\xi_m, \eta_m) = -1, \tag{21}$$

while for the gas subdomains (type (E)), we have

$$\beta \left(\frac{\partial^2 w_m}{\partial x^2}(\xi_m, \eta_m) + \frac{\partial^2 w_m}{\partial y^2}(\xi_m, \eta_m) \right) = \gamma_m \tag{22}$$

for the gas flow and

$$\int_{-1}^{1} \int_{-1}^{1} w_m(\xi_m, \eta_m) \frac{\mathrm{d}x}{\mathrm{d}\xi_m} \frac{\mathrm{d}y}{\mathrm{d}\eta_m} \, \mathrm{d}\xi_m \, \mathrm{d}\eta_m = 0 \tag{23}$$

for the flux constraint.

We solve these equation subject to boundary conditions (11), (12) and (13) in the transformed coordinate system, as well as additional conditions that enforce continuity of the velocity field and its first derivative between the liquid subdomains. Such conditions are necessary for convergence of the solution to a second-order PDE [18, 19]. Since only one condition can be applied on each side of a subdomain boundary, in the liquid subdomains, we enforce velocity continuity at $\xi = -1$ and continuity of its first derivative at $\xi = 1$. At the liquid-gas interface, we apply velocity continuity at $\eta = -1$ in the liquid and the shear stress conditions at $\eta = 1$ in the gas. Specific details of the boundary conditions for different domains are provided in Appendix A.

What has been described so far pertains to a channel with finite cross-section. For periodic grooves and infinite channels we can use the results given by setting $W = 2$ and changing the conditions (34) and (47) to

$$w_1(-1, \eta_1) = w_3(1, \eta_1) \tag{24}$$

$$\frac{\partial w_3}{\partial x}(1, \eta_3) = \frac{\partial w_1}{\partial x}(-1, \eta_3), \tag{25}$$

respectively, in order to enforce periodicity in the liquid velocity and its first derivative.

D. Discretization

To generate a numerical solution, we apply a Chebyshev collocation method to discretize the transformed equations and boundary conditions. We briefly describe the essential features of our approach here and refer the reader to standard texts [18–20] for more details.

In each subdomain, we solve for $(N+1) \times (N+1)$ values of the velocity field on the grid of Chebyshev points,

$$(\xi_i, \eta_j) := (\cos(i\pi/N), \cos(j\pi/N)) \tag{26}$$

for $i, j = 0, 1, \ldots N$, by imposing that the transformed equation is satisfied at the interior points ($i, j = 1, \ldots N-1$), and the boundary conditions are satisfied when either i or j is equal to 0 or N. As a result, the partial derivatives with respect to ξ and η appearing in the governing equations and boundary conditions are approximated by Chebyshev differentiation

matrices $D_N^{(\xi)}$ and $D_N^{(\eta)}$ (see references [18, 19]) respectively, that operate on a $(N+1)^2$ vector containing the unknown values of the velocity, w_{ij}, at the Chebyshev points. Along with these unknowns, we must also solve for the pressure gradient γ in the gas domains by enforcing a discrete version of the no-flux constraint Eq. (23),

$$\sum_{i=0}^{N}\sum_{j=0}^{N}\left[\frac{(1-\phi)(H/2-h_1(\xi_i))}{4}\right] w_{ij}^{(g)} a_i a_j = 0, \tag{27}$$

where a_i is the weight at node i of the Clenshaw-Curtis quadrature scheme (see Dahlquist et al. [21]). Note that the expression inside the square brackets is the Jacobian of the coordinate transform performed in the gas domain, and its inclusion allows us to compute the integral in ξ, η space.

Given the linearity of the equations, boundary conditions, and integral constraints, the discretized equations yield a linear system of equations for the values of the velocity and gas pressure gradients at all of the Chebyshev points in all of the subdomains. This system may be expressed as

$$\begin{pmatrix} \boldsymbol{A} & \boldsymbol{B} & \boldsymbol{0} \\ \boldsymbol{C} & \boldsymbol{D} & \boldsymbol{E} \\ \boldsymbol{0} & \boldsymbol{F} & \boldsymbol{0} \end{pmatrix} \begin{pmatrix} \boldsymbol{w}^{(l)} \\ \boldsymbol{w}^{(g)} \\ \boldsymbol{\gamma} \end{pmatrix} = \begin{pmatrix} \boldsymbol{G} \\ \boldsymbol{0} \\ \boldsymbol{0} \end{pmatrix} \tag{28}$$

where $\boldsymbol{w}^{(l)}$ is the vector containing the values of the velocity at the Chebyschev points in all of the liquid subdomains, $\boldsymbol{w}^{(g)}$ is the vector containing the values of the velocity at the Chebyschev points in all of the gas subdomains, and $\boldsymbol{\gamma}$ is the vector of gas pressure gradients. Thus, the matrix $\boldsymbol{A}$ arises due to the discretization of the equations in the liquid domains, as well as the boundary conditions imposed in these domains that couple the flows in neighbouring liquid subdomains; matrix $\boldsymbol{B}$ provides the coupling between the liquid and gas flows through the continuity boundary condition imposed in the liquid domains. In the second row, $\boldsymbol{C}$ is the coupling between the gas and liquid flows through the continuity of shear stress, $\boldsymbol{D}$ arises from discretizing the governing equations in the gas domains, and $\boldsymbol{E}$ links the gas pressure gradient to the governing equations. Finally, the matrix $\boldsymbol{F}$ arises by applying the quadrature scheme to the no-flux integral constraints in the gas domains and the vector $\boldsymbol{G}$ is equal to -1 if the row corresponds to the discretized equations for the flow, or 0 if the row is a boundary condition.

In our implementation, we build these matrices and vectors in MATLAB and solve the system directly using the backslash command. Since the coupling of the solution between subdomains only occurs through the boundary conditions, the matrices appearing in Eq. (28) are sparse. For finite channels with many periods, we only need to store the non-zero entries, leading to a substantial savings of memory.

E. Comments on the stress singularities

At the triple contact points, there are singularities in the gas and liquid velocity fields leading to infinite first derivatives. Solving the linear system given in (28) seems to give a convergent approximation to these velocity fields, and leads to far less oscillatory behaviour than a one-domain solution [19] (for the same number of nodes). However, some oscillations remain, and while the behaviour of the singularities is captured to a far greater extent than in one-domain solutions, not treating the singularities leads to slower convergence (as the number of nodes increases) and lower accuracy.

A more efficient approach is to treat the singularities in a semi-analytical way as we describe next. For the results given in section IV below, the singularities have been removed (and then reincorporated into the final solution), using a method similar to, but not identical to that described by Peyret [19]. In practice, this means that we solve numerically for $\widetilde{\boldsymbol{w}}^{(l)}$ and $\widetilde{\boldsymbol{w}}^{(g)}$, instead of $\boldsymbol{w}^{(l)}$ and $\boldsymbol{w}^{(g)}$, where

$$\widetilde{\boldsymbol{w}}^{(l)} = \boldsymbol{w}^{(l)} - \sum_{k=1}^{W} \alpha_k \boldsymbol{f}_k, \tag{29}$$

$$\widetilde{\boldsymbol{w}}^{(g)} = \boldsymbol{w}^{(g)} - \sum_{k=1}^{W} \alpha_k \boldsymbol{g}_k, \tag{30}$$

and α_k are singularity strengths to be found as part of the solution. The vectors $\boldsymbol{f}_k$ for the liquid and $\boldsymbol{g}_k$ for the gas contain the values of the singular parts of the respective velocity fields as detailed in Appendix B. Since the singularities in one gas domain do not directly contribute to the singularities in other gas domains, $\boldsymbol{g}_k$ is given the value 0 corresponding to positions in gas domains unaffected by the kth singularity. Hence, we add a new row and column to our matrix equation (28) for each unknown strength. The extra column acts to subtract the singular function from the problem, which in practice involves imposing the

boundary conditions (the singular functions satisfy the homogeneous Laplace equation) on the function, and subtracting the result from the appropriate part of the linear system. The extra row acts to impose an additional condition that the normal derivative at the point corresponding to the kth singularity (from the perspective of the subdomain above the gas-liquid interface) is zero. In practice, any condition that imposes a finite first derivative (not directed along the ridge) should suffice and alter the derived singularity strengths by a very small amount. This small alteration is acceptable as the final solution calculated is not particularly sensitive on the strengths of the singularity used [19]. We then solve the resultant linear system. In Appendix B we give the specific forms of the singular functions.

The method of finding the singularity strength by imposing that the normal derivative be equal to zero was found to perform well compared to two other methods attempted. The alternative methods were: (i) an iterative approach to minimize the value of the perturbation function in a small disk around the singularity - as in Peyret [19]; and (ii) an equivalent technique using an overdetermined matrix system and solved using MATLAB's backslash command to minimize the perturbation function in the disk as before. The derivative method we ultimately used was tested on the example case of singularity removal in Peyret [19], and the singularity strengths we derived were in very good agreement with those provided. The choice of the normal derivative was convenient since normal derivative conditions were already being used elsewhere on the meniscus, but otherwise arbitrary.

IV. VERIFICATION

We begin by assessing the accuracy of our method in capturing effects such as gas viscosity and meniscus curvature, by comparing with known results in the literature. When gas viscosity is included, but meniscus curvature is neglected, we compare against results from Maynes et al. [16] and Ng et al. [17]. In both of those studies, the channel is taken to be periodic and have dimensionless height $H = 2.8$, but the solid fraction and viscosity ratio are larger for Ng et al. [17] with $\phi = 0.25$ and $\beta = 0.01$, as compared to $\phi = 0.125$ and $\beta = 0.0097$ in Maynes et al. [16]. In Fig. 4(a) we show comparisons of the fluid velocity along the flat meniscus ($y = 0$) obtained by our computations and the studies mentioned above; the solid and dashed curves show our computations and superimpose the results of Maynes et al. [16] using open circles and those of Ng et al. [17] using triangles. For both cases, we see

very good agreement between our computations and those previously obtained. Note also that these results demonstrate that the velocity at the gas-liquid interface increases as the solid fraction decreases.

For the opposite scenario where meniscus curvature is present and gas viscosity is ignored, we compare our solutions with the asymptotic results of Sbragaglia and Prosperetti [14] and the numerical solutions obtained by Teo and Khoo [15] for the flow between a channel with one wall textured and the other a no-slip surface. Both studies give their results in terms of effective slip lengths, which are readily converted to flow rates (conversions are given in Equation 8 in either paper). Figure 4(b) shows the volumetric flow rate, Q, from those studies as a function of the protrusion angle θ, as well as the values from our computations. This shows very good agreement with the one-term asymptotic result of Sbragaglia and Prosperetti at small values of θ (less than approximately 0.5 radians, i.e., approximately 28 degrees) and for larger values of θ with Teo and Khoo's results and well within their maximum uncertainty of 0.5%. The computations also indicate that the flow rate increases with θ. This can be attributed to the fact that at small channel height-to-pitch ratios, typical in the results presented, the effect of an increased cross-sectional area outweighs the increase in shear stress at the ridge level.

We are also interested in the performance of our numerical framework. As shown in Fig. 5(a), with a 20th (or larger) order Chebyshev approximation, we can calculate Q to within 0.01%. Hence for the preceding calculations, this was deemed sufficient. However, for cases in which the problem is close to singular (for example where the meniscus approaches the opposite gas-solid interface), a higher order approximation was used for to accurately capture the solution. This was typically $N = 30$ or $N = 40$ as required.

This method is highly efficient. In Fig. 5(b) we give the time taken for a standard desktop computer to calculate the velocity field as we increase the width of the channel (and hence the number of subdomains) for $N = 20$.

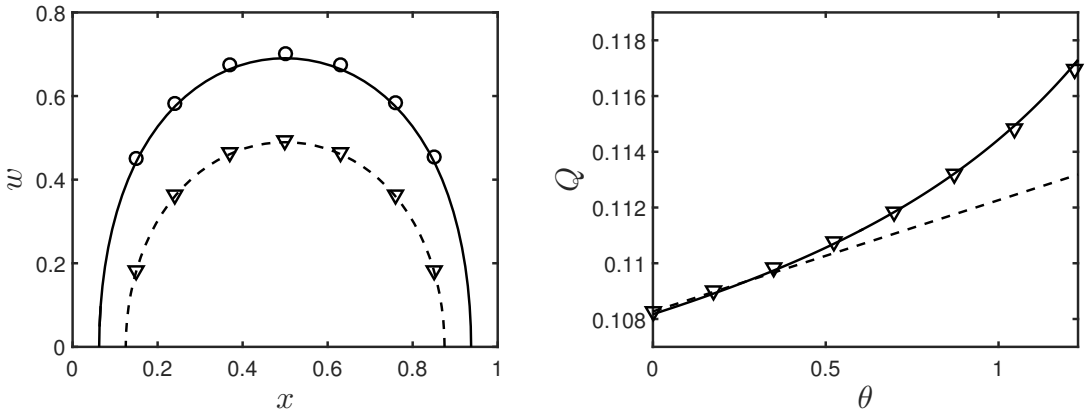

(a) (b)

FIG. 4: (a) The velocity at the liquid-gas interface against x for a periodic channel with $H = 2.8$, $\theta = 0$, and $\Delta = 0.4$. The solid curve shows our results and the circles show those from Maynes et al. [16] for $\phi = 0.125$ and $\beta = 0.0097$. Similarly, the dashed curve shows our results and the triangles are those from Ng et al. [17] for $\phi = 0.25$ and $\beta = 0.01$. (b) The volumetric flow rate as a function of θ for a periodic channel with $H = 1.5$, $\beta = 0$, $\Delta = 0.5$, $\phi = 0.5$. The solid curve corresponds to our results while the triangles give the values obtained by Teo and Khoo [15] and the dashed straight line was computed using the asymptotic formula from Sbragaglia and Prosperetti [14].

V. NUMERICAL RESULTS

A. Velocity field

We begin by performing computations to explore how the introduction of gas-filled grooves affects the flow in the channel. Figure 6 shows the velocity field in two periodic channels - contours of constant velocity are depicted in the figures. While both channels have a no-slip condition imposed on the upper boundary, the channel in panel 6(b) on the right has gas-filled grooves on the bottom boundary and that in panel 6(a) has another no-slip wall. The gas-liquid viscosity ratio is $\beta = 0.01$ and the meniscus is taken to be flat in this case. We see that the presence of the groove alters the parabolic flow found in the no-slip channel, compressing the lower value contours towards the triple contact points and increasing the liquid velocity near the centre of the cross section. For this case, the maximum

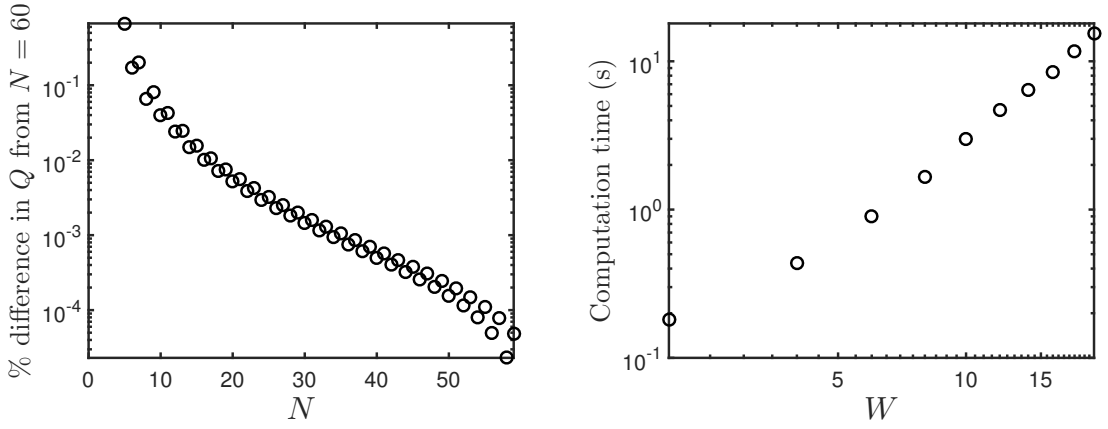

(a) (b)

FIG. 5: (a) The percentage difference between Q calculated with a 60th and Nth order Chebyshev approximation, given against N and computed in the periodic case (b) The time taken to compute the finite channel case for $N = 20$ given against W. Other parameter values in both cases are $\phi = 0.5$, $H = 2$, $\theta = 1$, $\Delta = 0.2$.

liquid velocity is increased by more than 30% due to the presence of the groove. The figure also illustrates the flow reversal in the gas region due to the induced pressure gradient that enforces a zero gas flux condition in the cross-section of the groove.

In periodic channels of infinite extent in the $x-$direction, the high velocity regions appearing above each liquid-gas interface will be identical by definition. In finite channels, however, the presence of side walls will affect the high velocity regions above grooves that are near these boundaries. Figure 7 shows the dimensionless velocity at the liquid-gas interface for a channel with four grooves ($W = 4$) along the upper and lower walls. Recall that, in the finite channel, the x coordinate is defined such that $x = 0$ corresponds to the left-most end wall; also, recall that lengths are non-dimensionalized with the groove period. Hence, the velocities for $0 < x < 1$ in Fig. 7 are those above the first groove, and $1 < x < 2$ the second groove. By symmetry, the interfacial velocity profiles above the third and fourth grooves are reflections of those shown for the second and first grooves respectively, about $x = 2$.

Figure 7(a) shows the computed velocity for different values of the contact angle θ and a passive gas region $\beta = 0$, while Fig. 7(b) shows the interfacial velocity for flat menisci and a range of viscosity ratios $\beta = 0, 0.01, 0.02$. Increasing β increases the interfacial shear stress

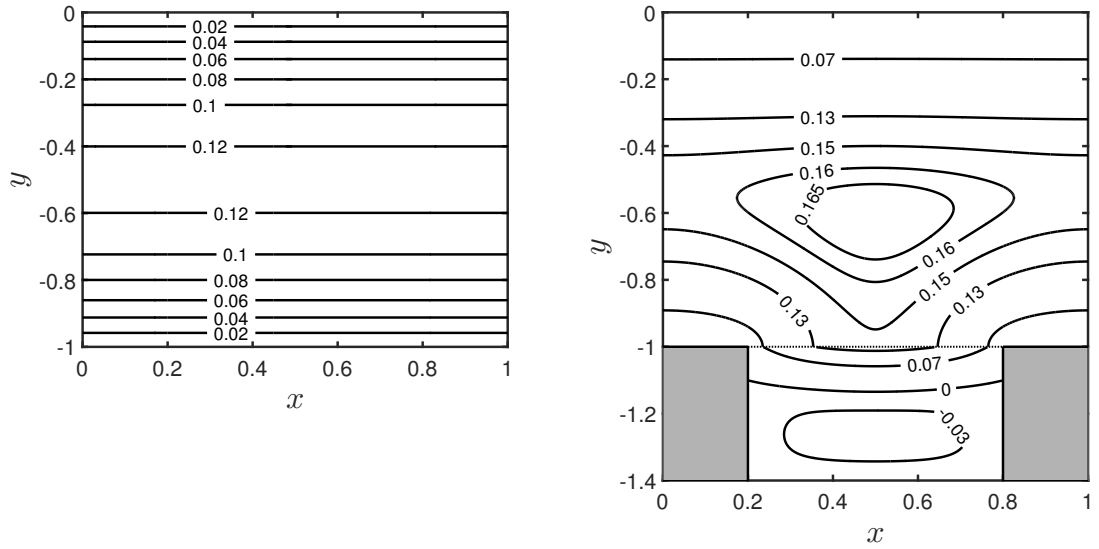

(a) (b)

FIG. 6: Velocity contours in (left) a no-slip channel and (right) a textured channel with $H = 1.4$, $\phi = 0.4$, $\Delta = 0.4$, $\beta = 0.01$ and $\theta = 0$. The grey regions indicate the ridges and the dotted line shows the gas-liquid interface.

and hence decreases the fluid velocity at the interface as seen in Fig. 7(b); the maximum velocity decreases by more than 10% when β is changed from 0 to 0.02. It is also seen from Fig. 7(a) that increasing θ also decreases the interfacial velocity at the centre of the groove, while increasing the interfacial velocity at either end. This increase in velocity towards the ends of the grooves can be explained mathematically by the increased strength in the contact line singularity at larger θ (see Appendix B). This phenomenon is explored in more depth by Kirk et al. [22] and Sbragaglia and Prosperetti [14]. These differences, however, are small compared to those due to the proximity of the groove to the end walls of the channel, as illustrated by both Fig. 7(a) and Fig. 7(b). We find that the velocity at the liquid-gas interface above the groove next to the end wall is approximately 40% less than that of its neighbour. Additionally, for each groove, the velocity profiles, which are symmetrical in the periodic case, now have a visible skew towards the centre of the channel. The asymmetry is more severe in the velocity profile for the interface closest to the end wall.

While there are dramatic changes in the fluid velocity profile near the end walls, it is

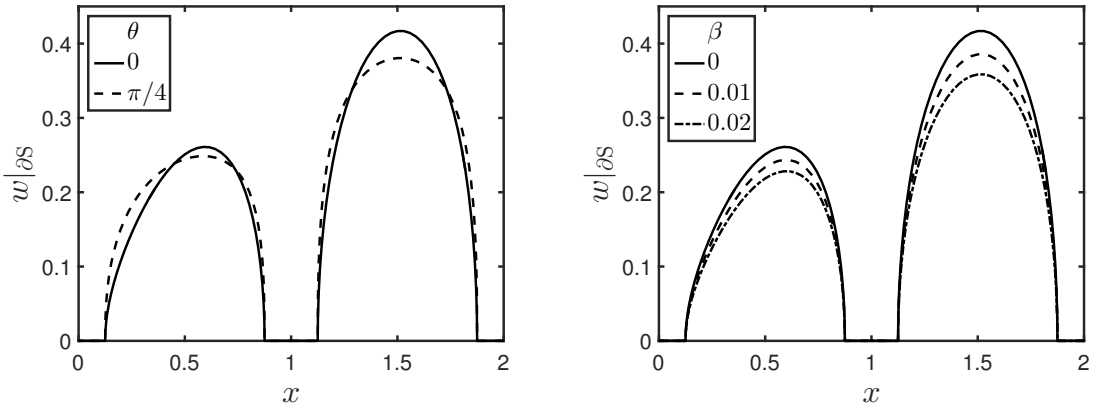

FIG. 7: Velocity profiles along the lower liquid boundary ($w|_{\partial S}$) for a channel with $H = 2.4$, $\Delta = 0.2$, $W = 4$, $\phi = 0.25$ and (a) $\beta = 0$ and the two indicated values of θ as well as (b) $\theta = 0$ and the three indicated values of β.

important to quantify how far these effects extend toward the centre of the channel, especially when the upper and lower walls possess many grooves. To fix matters and illustrate the effects, we pick a relatively wide channel of dimensionless width $W = 20$ that contains 20 symmetrically placed grooves on the upper and lower walls. The channel also has vertical sidewalls at $x = 0$ and $x = 20$. We proceed with a comparison of the flow in this channel with what would be obtained if the channel was of infinite horizontal extent with periodic grooves. We expect the periodic flow to coincide with the finite channel flow in the middle of a sufficiently wide channel. However, it is important for practical applications to quantify such differences since parameters, such as the channel height, can vary. We carry out a pointwise comparison by calculating the mean velocity in the liquid region averaged over y, i.e. we define $w_m(x) = \int_{y_l}^{0} w(x, y)\mathrm{d}y/|y_l(x)|$ where $y_l(x)$ is the position of the lower boundary (note that $y_l(x) < 0$) of the liquid region comprised of the union of the solid ridge surfaces and the liquid-gas interfaces. The mean velocity $w_m(x)$ is computed for the periodic as well as finite channel cases, and the results are compared in the form of a percentage decrease in the finite channel from the periodic groove case. Note that $w_m(0) = 0$ for the finite channel case since the origin is fixed at the left-most end wall - see Fig. 3. The percentage decrease from the periodic groove case is thus defined to be 100% there. The results are presented in

Fig. 8 - for a meniscus contact angle $\theta = \pi/10$, solid fraction $\phi = 0.5$, groove height $\Delta = 0.1$ and viscosity ratio $\beta = 0.01$ - for dimensionless channel heights H ranging from 1 to 16.

As expected, the percentage decrease reduces as we move towards the channel center, for all values of H. Observe that for small values of H/W the finite and periodic channel values become nearly identical a small distance away from the end wall. For example when $H = 1$ ($H/W = 1/20$) the percentage decrease is insignificant for $x > 2$, approximately, i.e., by the point when we are two grooves away from the end wall; for $H = 2$ ($H/W = 1/10$) we need to be at $x > 4$, approximately. For small values of H/W, therefore, the periodic model can provide an accurate characterization of the flow for a majority of the channel. As H/W increases, one must move further towards the centre of the channel to find regions where the finite and periodic channel velocities agree. For example, for $H = 4$ ($H/W = 1/5$) we need to be at $x > 6$, approximately, for the periodic channel to be in close agreement. Hence, for this height we have good agreement for less than half of the grooves. Once H becomes comparable to W, the finite and periodic calculations can give significantly different values across the entire channel. For instance, when $H = 8$ or 16 (i.e., $H/W = 2/5$ and $4/5$) we find that there is a difference of approximately 5% and 30%, respectively, in the middle of the channel.

Interestingly, repeating the results displayed in Fig. 8 but with a no-slip channel (of height 1, 2, 4, etc.) produces an almost identical figure. There are very minor differences in the $H = 1$ curve, but all of the other curves appear to be indistinguishable. Therefore, for these parameter values, we can obtain the range of validity of the periodicity assumption by studying instead the easier problem of a no-slip rectangular cross-section. This indicates that, for sufficiently large heights, edge effects and the effects of patterning are mostly decoupled. In theory, this may allow for the approximation of the mean velocity, and therefore the flow rate, in the finite channel, from the periodic channel using only knowledge from a no-slip rectangle. However, we expect it to be much harder to infer the flow field in the finite channel in this manner. We also expect the strength of this correspondence to reduce as the solid fraction reduces.

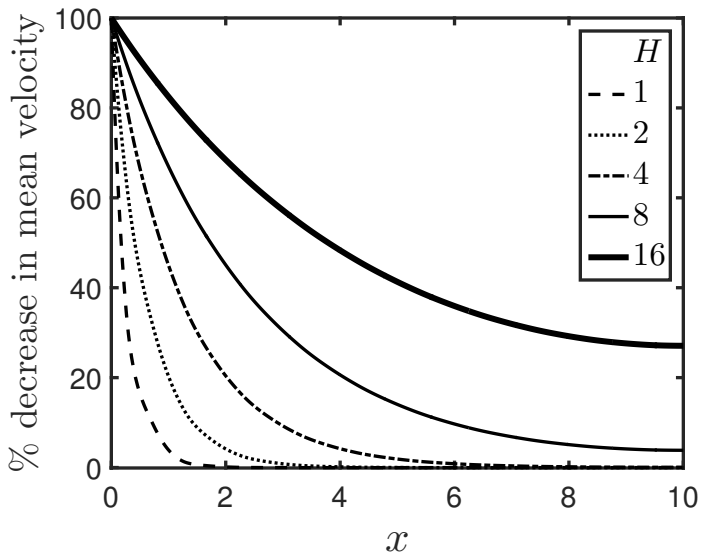

FIG. 8: The percentage decrease in mean velocity in a finite channel as compared to the periodic case, given against the spatial variable x. Parameter values are $\theta = \pi/10$, $W = 20$, $\phi = 0.5$, $\Delta = 0.1$, $\beta = 0.01$ and the five indicated values of H.

B. Normalized volumetric flow rate

In the previous section, we quantified how the introduction of gas-filled ridges can in general increase the velocity of the liquid. We are interested in evaluating how these changes in the velocity impact the overall flow rate for a given pressure gradient along the channel as we vary the solid fraction, meniscus curvature, and gas viscosity. To assess this, we focus on variations in the normalized volumetric flow rate

$$\bar{Q} = \frac{Q}{Q_{\text{no-slip}}}, \tag{31}$$

as the properties of the channel are changed. In expression (31), Q is the flow rate in the liquid, while $Q_{\text{no-slip}}$ is the flow rate through a no-slip channel of height H (see Fig. 1(b)). The latter is chosen for comparison, since in practical device applications there exist space constraints whether the channel is structured with gas-filled grooves or not; if the channel is not structured then the no-slip geometry for comparison purposes should be a channel of height H. For the periodic case it follows readily that $Q_{\text{no-slip}} = H^3/12$, while for finite channels the volumetric flow rate was computed numerically. Thus the quantity $\bar{Q}$ incorporates the cost of introducing solid regions to the no-slip channel to create the gas-

filled grooves to generate slip, but which reduce the liquid cross-sectional area. We require, then, that any velocity enhancement due to channel texturing must overcome the loss of liquid area to create the ridges. We find that by focusing on this quantity rather than the apparent slip length that is more commonly found in the literature, we can meaningfully quantify the effectiveness of gas lubrication in practical situations.

Note that, in the periodic case, it is straightforward to covert results for $\bar{Q}$ back into results for Q by multiplying by $H^3/12$. Results in terms of the apparent slip length can then be inferred, as well as different normalizations for the flow rate. For instance, it may be of interest to normalize by the flow rate through a no-slip channel of height $H - 2\Delta$, or a no-slip channel with a matching liquid cross-sectional area.

In what follows we examine the dependence of $\bar{Q}$ when one parameter is changed while keeping the others fixed. We first investigate variations in $\bar{Q}$ with solid fraction for finite cross-section channels having height to width ratio $H/W = 0.2$, and for flat menisci $\theta = 0$. The results are shown in Fig. 9 for different values of W - recall that an increase in W corresponds to an increase in the number of ridges on the upper and lower channel walls. We observe that regardless of the value of W, the ratio $\bar{Q}$ decreases as the solid fraction is increased, and converges to the same value of the normalized flow rate $\bar{Q} = 0.528$ as $\phi \to 1$. The value of $\bar{Q} = 0.528$ corresponds to the ratio of flow rates for two no-slip channels, one with height $H - 2\Delta$ and the other with height H.

The decrease in $\bar{Q}$ with increased solid fraction shown in Fig. 9 is expected; the results also indicate how to distribute the no-slip portion of the boundary in order to maximize $\bar{Q}$ for a given geometry. It can be seen from the results that for a fixed value of ϕ, higher flow rates are achieved when fewer large groves are used rather than many smaller ones. For example, when $W = 2$ we obtain $\bar{Q} = 1$ at $\phi \approx 0.65$, in which case most of the channel is a no-slip boundary. When $W = 8$, this does not occur until the solid fraction is as low as $\phi \approx 0.3$. For the lowest solid fractions shown, $\phi = 0.1$, we achieve values of $\bar{Q} > 4$ with $W = 2$ which is more than 2.5 times greater than the value found with $W = 8$.

In the remainder of the computations presented we concentrate on periodic channels with fixed height. This can be justified by assuming a sufficiently large width-height aspect ratio (a realistic assumption for the values of H considered) and referring to Fig. 8 that provides the computed differences in volumetric flux between finite and periodic geometries. By removing end-wall effects other physical effects can be elucidated in more detail. The

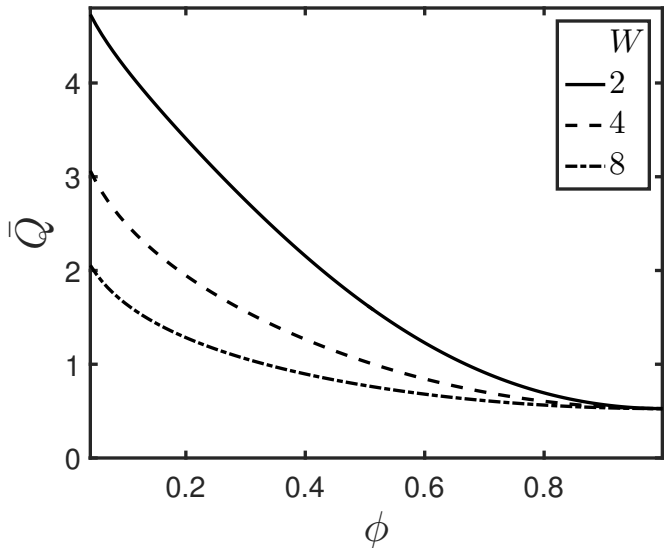

FIG. 9: The normalized flow rate as a function of ϕ for $H = W/5$, $\theta = 0$, $\Delta = W/50$, $\beta = 0.01$ and the three indicated values of W. Note that $\bar{Q}$ approaching a constant smaller than 1 as ϕ approaches 1 follows from our choice of normalization.

effect of ridge depth Δ and protrusion angle θ on the volumetric flow rate is investigated next. Figure 10(a) depicts the variation in $\bar{Q}$ as a function of the distance between the meniscus apex and the opposite gas-solid interface, defined by

$$\Delta_m = \Delta - \left(\frac{1-\phi}{2\sin\theta}\right)(1-\cos\theta). \tag{32}$$

The parameter Δ_m depends on both Δ and θ, the latter of which is kept constant on each curve. Using Δ_m instead of Δ in Fig. 10(a) ensures that the domain of all three curves is the same. Since H is held constant, increasing Δ (and hence Δ_m) results in a decrease in the size of the liquid domain. We see that for each value of θ, $\bar{Q}$ varies non-monotonically with Δ_m with maximum values occurring in the range $\Delta_m \approx 0.01 - 0.02$. For very small values of Δ_m, there is only a thin layer of gas between the liquid-gas interface and solid-gas surface at the bottom of the grooves. This leads to high values of gas-shear, which in turn slow down the flow in the liquid. As Δ_m is increased, the gas shear decreases, but this takes place at the expense of devoting more of the channel cross-section to create deeper ridges, which in turn tends to reduce $\bar{Q}$. The balance of these two effects produces the maxima in $\bar{Q}$ seen in Fig. 10(a). In contrast to the smaller meniscus protrusion angles, for the case of

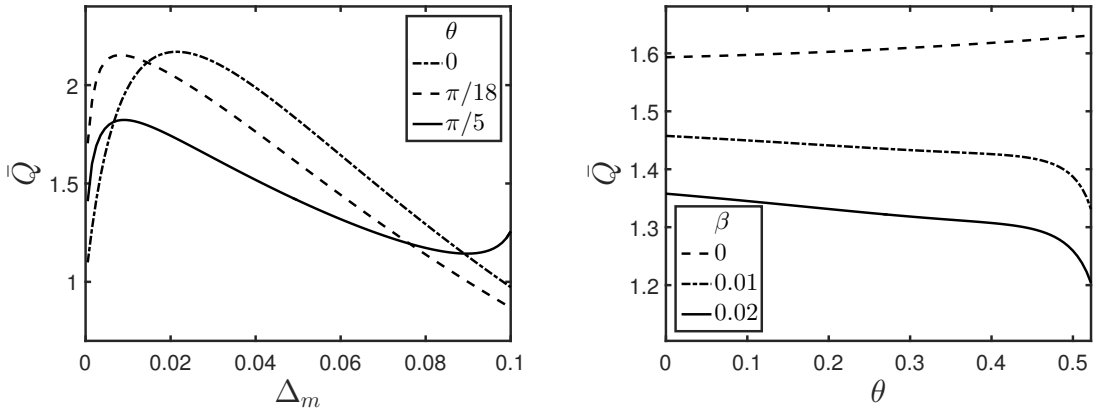

(a) (b)

FIG. 10: Effect of parameters on the normalized volumetric flow rate $\bar{Q}$: (a) variation of $\bar{Q}$ with Δ_m for $H = 0.4$, $\phi = 0.4$, $\beta = 0.01$ and the three indicated values of θ; (b) variation of $\bar{Q}$ with θ for $\phi = 0.2$, $\Delta = 0.11$, $H = 2$ and the three indicated values of β. Note that since the total channel height H is kept constant, varying Δ_m varies the liquid domain area, thus affecting the flow rate.

$\theta = \pi/5$ a minimum is found near $\Delta_m = 0.09$. Once again, it results from the balance of gas shear effects and the usage of area to create the ridges that yields this minimum. As $H - 2\Delta$ is very close to zero near this value of Δ_m, the solid-liquid boundaries on opposite sides of the channel nearly touch. As a result, most of the flowing liquid is above the liquid-gas boundaries, making gas shear important. Reducing the gas shear by increasing the gas depth leads to sufficiently higher flow rates to counteract the loss for liquid area.

The effect of meniscus protrusion angle θ on $\bar{Q}$ in a periodic channel, keeping all other parameters fixed, is shown in Fig. 10(b). While increasing θ will also inevitably decrease Δ_m, this takes place while keeping Δ fixed, in contrast to Fig. 10(a). Sbragaglia and Prosperetti [14] and Teo and Khoo [15] show that for sufficiently large height-period aspect ratios, meniscus protrusion can result in a decrease in flow rate, despite the liquid domain actually increasing in size. Their results also indicate that for the particular channel geometry considered in Fig. 10(b), we expect an increase in flow rate in the absence of gas viscosity, as verified by the $\beta = 0$ curve. However, we find that for $\beta = 0.01$ or 0.02, increasing the meniscus protrusion angle leads to a decrease in the volumetric flow rate. The reduction

in flow can hence be linked to gas shear, and highlights the importance of including gas viscosity in the model. For this case, we see that for most of the values of θ the decay is linear, however at around $\theta = 0.45$ the value of $\bar{Q}$ sharply decreases as the meniscus approaches the opposite gas-liquid interface. The effect of including gas viscosity is two-fold. First, increasing θ increases the length of the gas-liquid interface over which the shear stress in the gas acts to slow down the liquid. Second, as θ increases, Δ_m decreases, leading to higher values of interfacial shear-stress. The combination of these two effects can counteract that of an increased liquid domain that would ordinarily lead to an increase in flow rate.

Due to the large number of parameters present - see (1)-(5) - the computations presented above were used to quantify the effect on the flow in the structured channel as one parameter was varied and the others kept fixed. In what follows we extend the results by compiling two sets of contour plots of $\bar{Q}$ as a function of two parameters in each case. The first set considers variations of $\bar{Q}$ as the channel height H and the solid fraction ϕ are varied for fixed $\Delta = 0.1$ and $\theta = 0$, and viscosity ratios $\beta = 0$ and $\beta = 0.01$, respectively (Figs 11(a) and 11(b)). The second set of results fixes the channel height to $H = 2$ and the solid fraction to $\phi = 0.2$ and compiles the variation of $\bar{Q}$ with the meniscus protrusion angle θ and the ridge height Δ, again for viscosity ratios $\beta = 0$, 0.01 (Figs 12(a) and 12(b)). These parameters are of importance in practical applications and such results provide a quantitative basis for understanding the impact of gas-filled ridges on flow rates and the optimization of their effects.

Figures 11(a) and 11(b) show the contours of $\bar{Q}$ for periodic channels with heights in the range $0.3 \leq H \leq 8$ and solid fractions $0.1 \leq \phi \leq 0.9$. Results are shown for an inviscid gas cavity $\beta = 0$ and a typical gas-liquid viscosity ratio $\beta = 0.01$, respectively. We find, with the exception of very thin channels, that a channel characterized with solid fractions $\phi < 0.5$, yields volumetric flow rates $\bar{Q}$ greater than unity - i.e. the structured channel is more efficient in transporting liquid than the equivalent (larger cross-section) unstructured channel. The computations indicate that the largest enhancement occurs in the lower-left hand corners of Figs 11(a) and 11(b), where the solid fraction is very low and the channel is thin. However, the flow rate decreases to zero as $H \to 0.2$, which corresponds to a vanishing liquid region in this case. The results also show that the monotonic decrease in $\bar{Q}$ with ϕ documented in Fig. 9 appears to also hold for periodic channels and for all values of H. At higher values of ϕ, where the flow rate is smaller than that in the equivalent no-slip channel

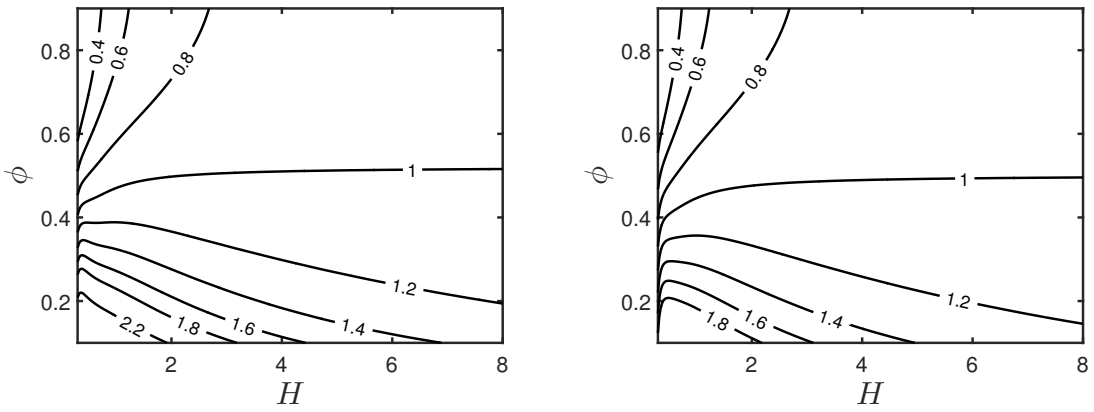

FIG. 11: Normalized flow rate contours, in the periodic case, as a function of H and ϕ with $\theta = 0$, $\Delta = 0.1$ and (a) $\beta = 0$, (b) $\beta = 0.01$.

of height H, the results indicate that an increase in H leads to a monotonic increase in $\bar{Q}$. For lower values of $\phi < 5$, however, where we have flow enhancement characterized by $\bar{Q} > 1$, we find that for fixed ϕ there can be a non-monotonic dependence of the flow rate on H for small values of H. For $\beta = 0.01$ for example shown in Fig. 11(b), the contours have local maxima at around $H \approx 0.5$, whereas for $\beta = 0$ shown in Fig. 11(a) this occurs at $H \approx 0.3$ which corresponds to a very small liquid domain. We can conclude, therefore, that in order to maximize flow rate, the channel should be designed to a solid fraction as low as possible, and the channel height should be about half the width of one period or smaller, i.e. $H \lessapprox 0.5$.

In Fig. 12(a) and Fig. 12(b), we show the contours of $\bar{Q}$ for viscosity ratios $\beta = 0$ and $\beta = 0.02$ respectively, and a range of θ and Δ, extending the results shown in Fig. 10(b). The other two parameters are fixed at $\phi = 0.2$ and $H = 2$. The shaded region indicates values of Δ and θ for which the liquid-gas interface intersects the solid-gas boundary, i.e., $\Delta_m \leq 0$. We find that in order to achieve flow enhancement, the ridge depth must be sufficiently low, which for this case requires $\Delta < 0.23$, approximately. It is found, then, that $\bar{Q}$ always decreases monotonically with θ as observed in Fig. 10(b). The results in Fig. 12(b) include gas viscosity, and we find now that for fixed values of θ, the flow rate $\bar{Q}$ depends non-monotonically on the ridge height Δ. As discussed earlier, this is linked to the competing

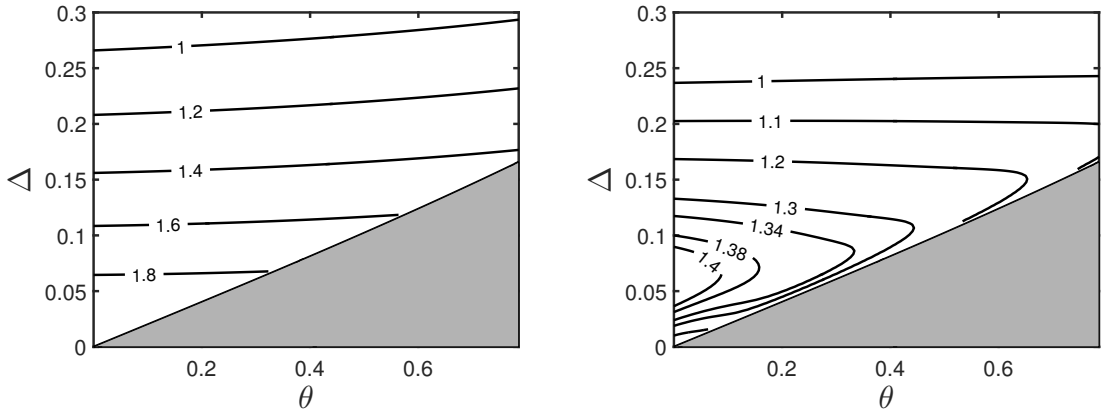

FIG. 12: Normalized flow rate contours, in the periodic case, as a function of θ and Δ with $\phi = 0.2$, $H = 2$ and (a) $\beta = 0$, (b) $\beta = 0.02$. The grey area is the parameter range for which the meniscus intersects the solid boundary. Note that since the total channel height H is kept constant, varying Δ varies the liquid domain area, thus affecting the flow rate.

factors of shear-stress along the meniscus and the relative size of the liquid domain. The results of Fig. 12(a) and Fig. 12(b) also indicate that varying Δ and θ appears to have a less dramatic effect on $\bar{Q}$ than changing the height or the solid fraction. Nonetheless, we can still find parameter values of θ and Δ that can increase the flow rate by more than 40%. The results indicate that the maximum increase in flow rate is achieved by minimizing the meniscus curvature (so as to minimize the shear stress in the gas) and having a small but finite value of the ridge height, which for this case is $\Delta \approx 0.06$. From Fig. 12(b) we also observe that, depending on the value of Δ, increasing the protrusion angle θ can either provide a modest increase in $\bar{Q}$ (for example $\Delta = 0.25$), or a decrease (for example $\Delta = 0.07$). By contrast, we see from Fig. 12(a) that for fixed values of Δ, $\bar{Q}$ monotonically increases with θ. This contrast can only be observed when accounting for both meniscus curvature and gas viscosity.

VI. CONCLUSIONS

We have presented a computationally efficient numerical framework based on Chebyschev collocation that allows us to study the combined effects of gas viscosity, meniscus curvature, and finite channel cross-sections on liquid flows through textured microchannels. A key aspect of this method is the combined usage of domain decomposition and singularity removal to accurately capture singularities in the flow due to the abrupt change in boundary conditions at the triple contact points, along with coordinate transformations to handle meniscus curvature. Using this method, we quantified the validity of the commonly used periodic channel assumption, showing that it yields an accurate characterization of the flow away from the end walls in very flat channels, but breaks down when the channel height is comparable to the channel width. Furthermore, we explored in detail how the normalized flow rate through these channels varies with the parameters governing channel aspect ratio, solid fraction, height of the gas ridges, and meniscus curvature. In particular, we showed that the normalized flow rate can vary non-monotonically with the cavity height, and can increase with meniscus protrusion in the absence of gas viscosity but decrease with meniscus protrusion in its presence. Both of these results are linked to the effect of shear stress on the liquid-gas interface, highlighting the importance of including gas viscosity in the models and capturing the flow in the gas. Finally, these results suggest several important principles that can be useful in optimizing flow enhancement: these include constructing channels with fewer, wider grooves while aiming to minimize meniscus curvature; the groove depth should be carefully chosen to be sufficiently small so as to maximize the area taken up by the liquid, but deep enough to minimize the effects of gas shear stresses.

While our model incorporates many of the features present in real textured channel flows, there are still several assumptions that may be relaxed. For example, our model assumes the atomistic nature of the gas can be ignored and coupling to the liquid flow can be described by a no-slip condition. Specifically, we have assumed that the Knudsen number,

$$Kn = \frac{\ell}{L}, \tag{33}$$

where ℓ is the mean free path of the gas and L is a representative physical length scale (e.g. the groove depth or width), is very low, $Kn \ll 1$. Small Knudsen number effects can readily be incorporated into our model by introducing a Navier slip condition at the gas

boundaries to capture molecular slip [23]. Perhaps more importantly, in experiments the meniscus curvature is itself nor prescribed, but is set by the inlet and outlet pressures and will vary along the length of the channel. Thus, the geometry of the liquid domain becomes coupled to the pressure variation along the channel and would need to be determined as part of a full three-dimensional computation. Consequently, the two-dimensional results presented here are indicative of the flow resistance encountered at various points along the three-dimensional channel (assuming the meniscus curvature varies sufficiently slowly), rather than being predictive of the flow rate through it. We expect this limitation to be particularly relevant for channels of small heights, in which changes to meniscus geometry are of greater relative importance. Additionally, the numerical approach we have used in this study can also can be applied to the equations that include heat and/or mass transport in textured channels. This model could then be used to better understand, or even optimize, the usage of patterned channels in microprocessor cooling applications.

APPENDIX A: DETAILS OF BOUNDARY CONDITIONS BETWEEN DECOMPOSED DOMAINS

Here we provide details of the boundary conditions imposed at the ends of each type of subdomain described in section III C.

Specifically, the boundary conditions for the subdomain of type (A) are

$$w_1(-1, \eta_1) = 0 \tag{34}$$

$$\frac{\partial w_1}{\partial x}(1, \eta_1) = \frac{\partial w_2}{\partial x}(-1, \eta_1) \tag{35}$$

$$w_1(\xi_1, -1) = 0 \tag{36}$$

$$\frac{\partial w_1}{\partial y}(\xi_1, 1) = 0 \tag{37}$$

respectively corresponding to no-slip, continuity of the x derivative between subdomains 1 and 2, no-slip and symmetry (in the y direction).

For subdomains of type (B) we have

$$w_m(-1, \eta_m) = w_{m-1}(1, \eta_m) \tag{38}$$

$$\frac{\partial w_m}{\partial x}(1,\eta_m) = \frac{\partial w_{m+1}}{\partial x}(-1,\eta_m) \tag{39}$$

$$w_m(\xi_m,-1) = w_{(W+1+m/2)}(\xi_m,1) \tag{40}$$

$$\frac{\partial w_m}{\partial y}(\xi_m,1) = 0 \tag{41}$$

respectively corresponding to continuity of velocity between subdomains m and $m-1$, continuity of the x derivative between subdomains m and $m+1$, continuity of velocity on the liquid-gas interface and symmetry (in the y direction).

For subdomains of type (C) we have

$$w_m(-1,\eta_m) = w_{m-1}(1,\eta_m) \tag{42}$$

$$\frac{\partial w_m}{\partial x}(1,\eta_m) = \frac{\partial w_{m+1}}{\partial x}(-1,\eta_m) \tag{43}$$

$$w_m(\xi_m,-1) = 0 \tag{44}$$

$$\frac{\partial w_m}{\partial y}(\xi_m,1) = 0 \tag{45}$$

respectively corresponding to continuity of velocity between subdomains m and $m-1$, continuity of the x derivative between subdomains m and $m+1$, no-slip and symmetry (in the y direction).

For the subdomain $(W+1)$ of type (D) we have

$$w_{W+1}(-1,\eta_{W+1}) = w_W(1,\eta_{W+1}) \tag{46}$$

$$\frac{\partial w_{W+1}}{\partial x}(1,\eta_{W+1}) = 0 \tag{47}$$

$$w_{W+1}(\xi_{W+1},-1) = 0 \tag{48}$$

$$\frac{\partial w_{W+1}}{\partial y}(\xi_{W+1},1) = 0 \tag{49}$$

respectively corresponding to continuity of velocity between subdomains $W+1$ and W, symmetry (in the x direction), no-slip and symmetry (in the y direction).

For subdomains of type (E) we have

$$w_m(-1,\eta_m) = 0 \tag{50}$$

$$w_m(1,\eta_m) = 0 \tag{51}$$

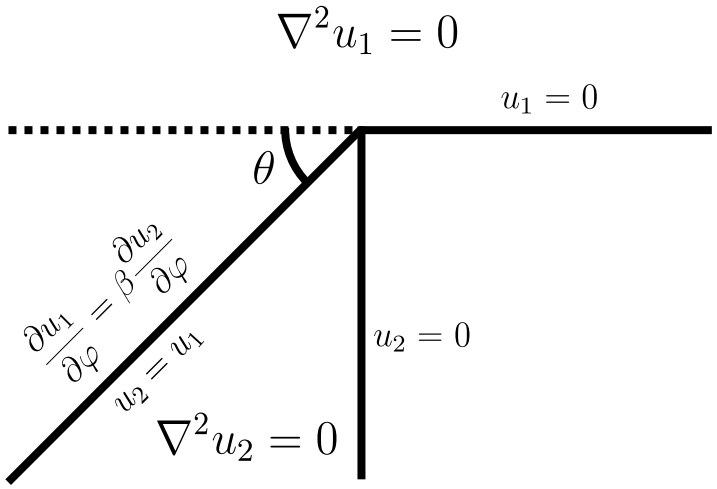

FIG. 13: The equations and boundary conditions satisfied by the singular parts of the velocity fields

$$w_m(\xi_m, -1) = 0 \tag{52}$$

$$\beta \frac{\partial w_m}{\partial n}(\xi_m, 1) = \frac{\partial w_{(2m-2M-2)}}{\partial n}(\xi_m, -1) \tag{53}$$

respectively corresponding to no-slip (first three) and continuity of shear stress on the gas-liquid interface.

APPENDIX B: SINGULARITY REMOVAL

The singular parts of the velocity field satisfy the equations and boundary conditions illustrated in Fig. 13. It can be shown by separation of variables in polar coordinates (defined using the singularity location as the origin) that the general form of the solution is:

$$u_1 = \alpha r^\lambda \sin \lambda\varphi \tag{54}$$

$$u_2 = \alpha \frac{\sin\left(\lambda(\pi + \theta)\right)}{\sin\left(\lambda(\pi/2 - \theta)\right)} r^\lambda \sin\left(\lambda(3\pi/2 - \varphi)\right) \tag{55}$$

where r is the radial coordinate and φ is the angular coordinate (with the anticlockwise direction as positive and the ridge as $\varphi = 0$) and $0 < \lambda < 1$ is found numerically from

$$\beta \sin\left(\lambda(\pi + \theta)\right) \cos\left(\lambda(\theta - \pi/2)\right) = \cos\left(\lambda(\pi + \theta)\right) \sin\left(\lambda(\theta - \pi/2)\right) \tag{56}$$

The singular functions corresponding to singularities on the left of the groove (rather than the right as shown above) can be found by reflecting the solution above in x.

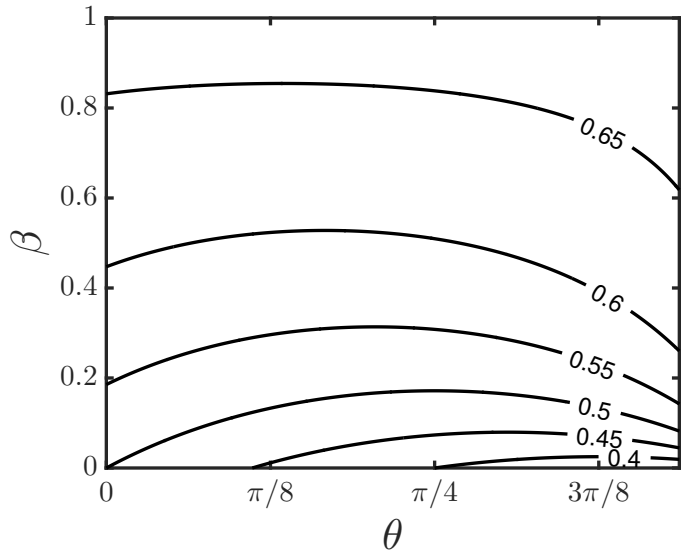

FIG. 14: The singularity exponent λ given as a function of the viscosity ratio β and the protrusion angle θ.

In Fig. 14, we provide contour plots of the singularity exponent λ against θ and β. Note that while the presence of a small viscosity ratio $\beta \approx 0.02$ can have a significant effect of the flow rate (see Fig. 10(b), for example), it has limited impact on the singularity exponent. Hence, for applications such as those in the present paper, good accuracy can be achieved by making the approximation $\lambda \approx \pi/[2(\pi + \theta)]$, which results from setting $\beta = 0$ in (56). It is interesting to note that gas viscosity always increases the singularity exponent (making the profile less singular) while the protrusion angle generally decreases the exponent (making the profile more singular).

ACKNOWLEDGEMENTS

S.E.G. acknowledges support of an Imperial College President's PhD Scholarship. M.H. was supported in part by NSF grant no. 1402783. The work of D.T.P. was supported in part by EPSRC grants EP/K041134/1 and EP/L020564/1. We also want to thank Prof. Darren Crowdy for some interesting discussions.

REFERENCES

[1] J. P. Rothstein, "Slip on superhydrophobic surfaces," *Annual Review of Fluid Mechanics*, vol. 42, pp. 89–109, 2010.

[2] W. Barthlott and C. Neinhuis, "Purity of the sacred lotus, or escape from contamination in biological surfaces," *Planta*, vol. 202, no. 1, pp. 1–8, 1997.

[3] X.-M. Li, D. Reinhoudt, and M. Crego-Calama, "What do we need for a superhydrophobic surface? a review on the recent progress in the preparation of superhydrophobic surfaces," *Chemical Society Reviews*, vol. 36, no. 8, pp. 1350–1368, 2007.

[4] L. S. Lam, M. Hodes, and R. Enright, "Analysis of galinstan-based microgap cooling enhancement using structured surfaces," *Journal of Heat Transfer*, vol. 137, no. 9, p. 091003, 2015.

[5] C. Lee and C.-J. Kim, "Underwater restoration and retention of gases on superhydrophobic surfaces for drag reduction," *Physical Review Letters*, vol. 106, no. 1, p. 014502, 2011.

[6] M. Xu, G. Sun, and C.-J. Kim, "Infinite lifetime of underwater superhydrophobic states," *Physical review letters*, vol. 113, no. 13, p. 136103, 2014.

[7] J. Ou, B. Perot, and J. P. Rothstein, "Laminar drag reduction in microchannels using ultrahydrophobic surfaces," *Physics of Fluids (1994-present)*, vol. 16, no. 12, pp. 4635–4643, 2004.

[8] J. R. Philip, "Flows satisfying mixed no-slip and no-shear conditions," *Zeitschrift für angewandte Mathematik und Physik ZAMP*, vol. 23, no. 3, pp. 353–372, 1972.

[9] J. R. Philip, "Integral properties of flows satisfying mixed no-slip and no-shear conditions," *Zeitschrift für angewandte Mathematik und Physik ZAMP*, vol. 23, no. 6, pp. 960–968, 1972.

[10] E. Lauga and H. A. Stone, "Effective slip in pressure-driven stokes flow," *Journal of Fluid Mechanics*, vol. 489, pp. 55–77, 2003.

[11] C. Teo and B. Khoo, "Analysis of stokes flow in microchannels with superhydrophobic surfaces containing a periodic array of micro-grooves," *Microfluidics and nanofluidics*, vol. 7, no. 3, pp. 353–382, 2009.

[12] J. Ou and J. P. Rothstein, "Direct velocity measurements of the flow past drag-reducing ultrahydrophobic surfaces," *Physics of Fluids (1994-present)*, vol. 17, no. 10, p. 103606, 2005.

[13] P. Tsai, A. M. Peters, C. Pirat, M. Wessling, R. G. Lammertink, and D. Lohse, "Quantifying effective slip length over micropatterned hydrophobic surfaces," *Physics of Fluids (1994-present)*, vol. 21, no. 11, p. 112002, 2009.

[14] M. Sbragaglia and A. Prosperetti, "A note on the effective slip properties for microchannel flows with ultrahydrophobic surfaces," *Physics of Fluids (1994-present)*, vol. 19, no. 4, p. 043603, 2007.

[15] C. Teo and B. Khoo, "Flow past superhydrophobic surfaces containing longitudinal grooves: effects of interface curvature," *Microfluidics and Nanofluidics*, vol. 9, no. 2-3, pp. 499–511, 2010.

[16] D. Maynes, K. Jeffs, B. Woolford, and B. Webb, "Laminar flow in a microchannel with hydrophobic surface patterned microribs oriented parallel to the flow direction," *Physics of Fluids (1994-present)*, vol. 19, no. 9, p. 093603, 2007.

[17] C.-O. Ng, H. C. Chu, and C. Wang, "On the effects of liquid-gas interfacial shear on slip flow through a parallel-plate channel with superhydrophobic grooved walls," *Physics of Fluids (1994-present)*, vol. 22, no. 10, p. 102002, 2010.

[18] C. Canuto, M. Y. Hussaini, A. Quarteroni, and T. A. Zang, "Spectral methods in fluid dynamics," ch. 13, 1988.

[19] R. Peyret, *Spectral methods for incompressible viscous flow*, vol. 148. Springer Science & Business Media, 2013.

[20] L. N. Trefethen, *Spectral methods in MATLAB*, vol. 10. Siam, 2000.

[21] G. Dahlquist and Å. Björck, "Numerical methods in scientific computing, volume i," 2007.

[22] T. L. Kirk, M. Hodes, and D. T. Papageorgiou, "Nusselt numbers for poiseuille flow over isoflux parallel ridges accounting for meniscus curvature," *Journal of Fluid Mechanics*, vol. 811, pp. 315–349, 2017.

[23] L. M. Jiji, *Heat convection*. Springer.